Fuel 381 (2025) 133147

Contents lists available at ScienceDirect

Fuel

journal homepage: www.elsevier.com/locate/fuel

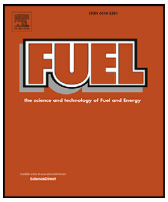

Full length article

Oxidation progress and inner structure during single micron-sized iron particles combustion in a hot oxidizing atmosphere

Anton Sperling [a], Max P. Deutschmann [b], Daoguan Ning [a,*], Jonas Spielmann [c], Tao Li [a], Ulrike I. Kramm [c], Hermann Nirschl [b], Benjamin Böhm [a], Andreas Dreizler [a]

[a] Technical University of Darmstadt, Department of Mechanical Engineering, Reactive Flows and Diagnostics, Otto-Berndt-Str. 3, Darmstadt, 64287, Germany
[b] Karlsruhe Institute of Technology, Institute of Mechanical Process Engineering and Mechanics, Process Machines, Strasse am Forum 8, Karlsruhe, 76131, Germany
[c] Technical University of Darmstadt, Department of Chemistry, Catalysts and Electrocatalysts Group, Otto-Berndt-Str. 3, Darmstadt, 64287, Germany

ARTICLE INFO

Keywords:
Metal fuel
Inner particle structure
Liquid phase iron oxidation
Single iron particle oxidation

ABSTRACT

The present experimental study focuses on the determination of the oxidation progress and internal structures during the combustion of single iron particles using combined *in-situ* optical measurements and *ex-situ* material examination of rapidly quenched particles. Narrowly sieved iron particles with a mean diameter of 49 μm are ignited and burn in the hot exhaust of a premixed $CH_4/O_2/N_2$ flat flame with remaining 20 vol% O_2, provided by a laminar flow reactor with well-defined thermal and flow boundary conditions. During particle combustion, key parameters of oxidation progress are determined optically in a time-resolved manner, such as the time-resolved particle surface temperature and the reaction time relative to the instant of the particle peak temperature. Furthermore, individually burning particles are rapidly quenched at different combustion stages and then extracted from the exhaust gas using an isokinetic extraction probe. The bulk composition of the quenched particles with respect to α-Fe and its three oxides FeO, Fe_3O_4, and Fe_2O_3 is determined using Wide-angle X-ray Scattering and ^{57}Fe Mössbauer Spectroscopy. Combining the information obtained from *in-situ* and *ex-situ* measurements, it is shown that iron particles oxidize rapidly to FeO during the initial stage of combustion, followed by a much slower oxidation to Fe_3O_4 as the particles cool down. The peak particle temperatures are measured during the fast initial oxidation. Finally, particles sampled from representative positions of the oxidation process are analyzed by Energy-Dispersive X-ray Spectroscopy and Focused Ion Beam Scanning Electron Microscopy, revealing different particle morphology and internal structures. For the first time, the clear presence of an oxide shell and iron-core structure in quenched particles suggests that liquid iron and liquid iron oxide are layered during liquid phase combustion, if the particle remains within the miscible gap.

1. Introduction

Iron powder has been proposed as a promising carbon-free energy carrier due to many inherent advantages, e.g., abundance, high specific energy, and potential recyclability [1]. It has the potential to overcome the intermittency and geographical dispersion of clean power produced by solar, wind, and hydro power. The retrofitting of coal-fired power plants with iron powders paves a way for the reliable generation of green electricity on demand. Attributed to the non-volatile characteristic of iron particle combustion, iron dust flames exhibit unique features, such as low sensitivity of reaction wave velocities to equivalence ratio [2]. A comprehensive understanding and quantitative prediction of pulverized iron flames are essential to developing industry-scale combustion devices, for which multi-dimensional and multi-scale computational fluid dynamic (CFD) simulations are needed. To overcome the present limitation in prediction, one building block is a more detailed understanding of high-temperature iron particle oxidation. Due to the well-defined boundary conditions, as a first step, fundamental studies of single iron particle oxidation emerged as an important research approach. In addition, understanding the changes in the particle's structure upon oxidation is a useful step towards improving the recyclability of the fuel.

A number of fundamental studies have advanced considerably the understanding of single iron particle combustion, by focusing on the global oxidation time scales [3,4], temporal particle temperature evolution [5,6], and *ex-situ* morphological analysis [7,8]. Also, the influence of CO onto the reaction of iron particles combusting in premixed

---

* Corresponding author.
E-mail address: ning@rsm.tu-darmstadt.de (D. Ning).

https://doi.org/10.1016/j.fuel.2024.133147
Received 10 May 2024; Received in revised form 2 September 2024; Accepted 12 September 2024
Available online 27 September 2024

methane flames have been investigated, indicating that even very small levels of CO increase the probability of micro-explosions for iron particles up to 50 μm [9]. However, detailed investigations into the oxidation progress and internal structures during single iron particle combustion are rarely conducted. The first attempt to characterize the internal structures and oxidation levels of combusted iron particles was reported by Choisez et al. [10]. *Ex-situ* material characterization of iron oxide particles collected from a turbulent burner was performed. Complex morphology, microscopic structure, and different oxidation levels were observed. Despite the rich details revealed from that work, the oxidation state at the different stages of iron particle combustion still remains elusive due to the challenges of accurately quenching particle combustion at the desired location and reaction time in a turbulent flow. To this end, the rapid termination of the combustion process and the extraction of quenched particles under well-controlled thermal and fluid dynamical conditions, e.g., isothermal and laminar, are highly desirable. Previously, rapid quenching of burning metal particles was demonstrated to be a powerful technique to *in-situ* freeze the oxidation progress, enabling sophisticated *ex-situ* characterization of the oxidation state and internal structure of the particles [11].

In this work, we performed *in-situ* rapid quenching and sampling of micron-sized iron particles at different oxidation stages under precisely controlled conditions. At the sampling position, the reaction progress of the particles was characterized by time-resolved two-color pyrometry measurement of the particle temperature. The composition of the sampled particles was quantified using ^{57}Fe Mössbauer spectroscopy (MS) and Wide-Angle X-ray Scattering (WAXS). The morphology of the quenched particles was examined by Focused Ion Beam - Scanning Electron Microscopy (FIB-SEM). The combined *in-situ* and *ex-situ* diagnostics allow a detailed characterization of the micro-structures and the oxidation states during the tens of milliseconds combustion process of micron-sized iron particles. To the best of the authors' knowledge, this is the first report on the time-resolved oxidation progress of burning single iron particles.

The structure of this work is as follows: In Section 2 the experimental setup and the iron particles used are presented and characterized. The measurement techniques are then described: two-color pyrometry, MS, WAXS, (FIB-)SEM, and energy dispersive X-ray spectroscopy (EDX). In Section 3, first the results of the overall oxidation progress are presented and discussed. Hereafter, the oxide-resolved composition of the quenched particles is presented and discussed, followed by a discussion of the observed morphology at selected sampling positions (SP). Next, the oxidation trajectory is mapped onto the Fe–O phase diagram and interpreted. The final Section 4 concludes the results of this work.

2. Experimental methodology

2.1. Reactor and operational conditions

To study the iron oxidation progress in hot oxidizing flows, as shown in Fig. 2, combined *in-situ* measurement methods including rapid quenching, sampling, and optical thermometry were applied for micron-sized iron particles at different combustion stages in a laminar flow reactor (LFR). A premixed $CH_4/O_2/N_2$ flat flame was stabilized on a ceramic matrix burner, generating a hot laminar oxidizing atmosphere for particle ignition and combustion. A residual oxygen volume fraction of $20\,\%_{\mathrm{vol}}$ in the exhaust gas was determined using 1D free-propagation flame simulations in Cantera. The burner was enclosed by a fused silica chimney, providing well-characterized gas velocities and temperature profiles along the burner center line [12].

Isolated particles were introduced into the LFR using a carrier gas of pure N_2 through a particle dispersion unit. In this unit, an impeller creates a particle dispersion. A small N_2 gas stream carries individual particles from the dispersion through a $D_{inner} = 0.8\,\mathrm{mm}$ injection tube into the LFR. The seeding rate can be adjusted by the impeller speed, the particle loading and by slight changes in the gas flow rate through the injection tube. The terminal gas velocity in the LFR was approximately 1.67 m/s. The gas temperature in the center of the burner was measured previously using quantitative laser-induced fluorescence of the OH radical (OH-LIF) combined with absorption spectroscopy [12]. The initial gas temperature was determined to be 1877 K at 2.5 mm height above the burner (HAB), which decreased to 1760 K in the beginning of the region shown in Fig. 5(b)(−11 ms) and cooled further towards the end of the shown region (30 ms).

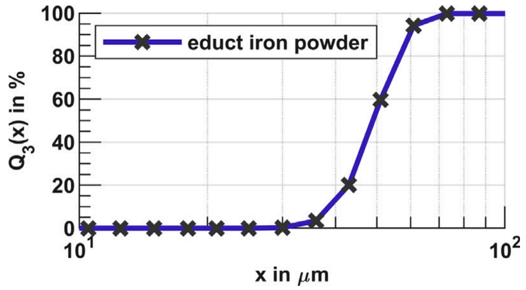

Fig. 1. Particle size distribution (Q3) of the investigated iron particles.

Particle extraction at different stages of combustion was precisely adjusted by positioning the extraction probe at different HABs. The composition of the partially oxidized particles probed at different HAB was then independently analyzed *ex-situ* using several material characterization techniques. The temperature trajectory of the particles was determined using two-color pyrometry, accomplished after removing the extraction probe. The individual parts of the experiment are described in more detail in the next sections.

2.2. Characterization of the used iron particles

Iron particles produced by inert gas atomization from Eckart TLS, Germany, with a purity of 99.8 % were used. The particles were chosen due to their near-spherical shape and the lack of visible pores making them easier to model from a CFD perspective. The particles were sieved (sieve size: 45–50 μm) and the mean particle size Q3 was determined to be 49 μm using static laser diffraction analysis (HELOS QUIXEL). The particle size distribution after sieving is shown in Fig. 1. The oxygen content of the virgin particles was below the detection limits of WAXS or MS. A SEM image of the educt particles is shown in Fig. 7 (0).

2.3. Particle quenching and sampling

Particles were rapidly quenched and extracted from the hot oxidizing environment by adding an isokinetic particle extraction probe to the LFR. The LFR was moved to sample at different locations which were selected based on the luminescence of the particle streaks with refined increments near the maxima and are as follows: 25, 28, 33, 38, 43, 48, 88, 137 and 186 mm HAB.

The extraction probe is based on a modified design used by Tarlinski et al. [13] as illustrated in Fig. 2(a). Using a vacuum pump, burning particles were extracted together with the exhaust gas, which is then diluted by a nitrogen flow ($3.8–4\,\mathrm{m_n^3/h}$) to contain below $1.7\,\%_{\mathrm{vol}}$ O_2 and cooled down with an integrated water cooling system. The particles were collected by a polyethylene (PE) filter (nominal pore size 5 μm) installed at the end of the 900 mm (d_f) long probe. To ensure isokinetic sampling and to minimize the residual oxygen inside the extraction probe, the sampled exhaust gas was highly diluted by adjusting the nitrogen flow rate so that individual particles were slightly decelerated just upstream of the probe inlet.

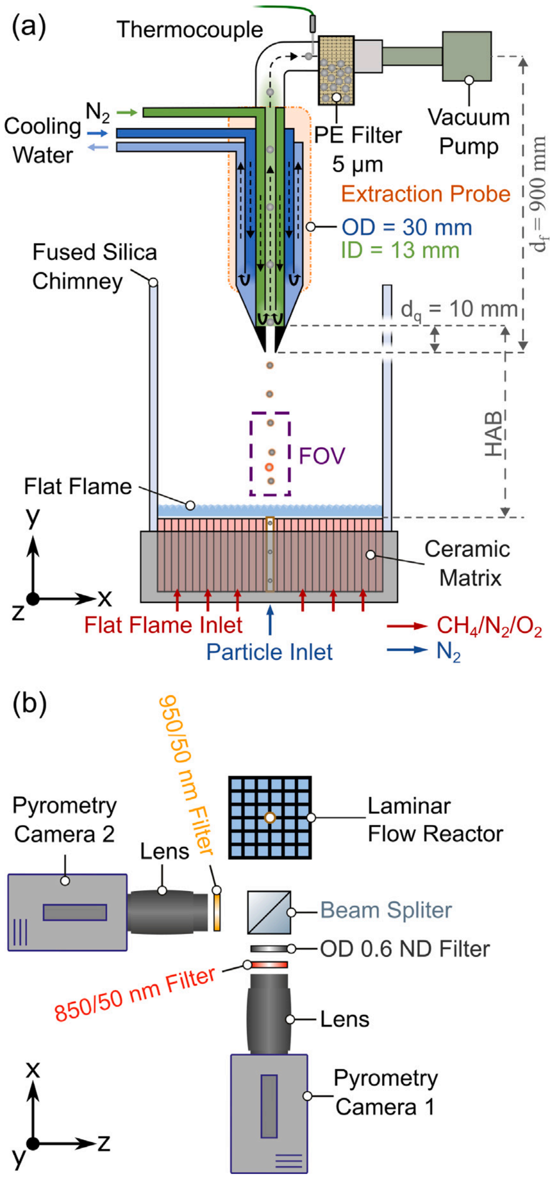

Fig. 2. (a) Schematic setup used to extract the particles from the LFR. (b) Optical setup of the two-color pyrometry measurements (without extraction probe) for particle temperatures and velocities' in the FOV marked in (a).

2.4. *Characterization of the particle extraction*

Particle extraction was conducted for one hour at each sampling location, yielding 80–100 mg of partially oxidized iron particles. The particle number density just before the probe inlet was monitored with a high-speed camera to ensure that the inter-particle distance was larger than 10 particle diameters. Therefore, the oxidation of a single particle is independent of the influence of other particles and inter-particle collisions are unlikely. An exemplary photograph of the particle streaks is given in Fig. 3.

Fig. 3. Exemplary photographs of particle streaks. The methane flat flame and the tip of the extraction lance can be seen. The edges of the extraction lance are highlighted. The extraction position is at 186 mm HAB. The exposure time is 1/40 s.

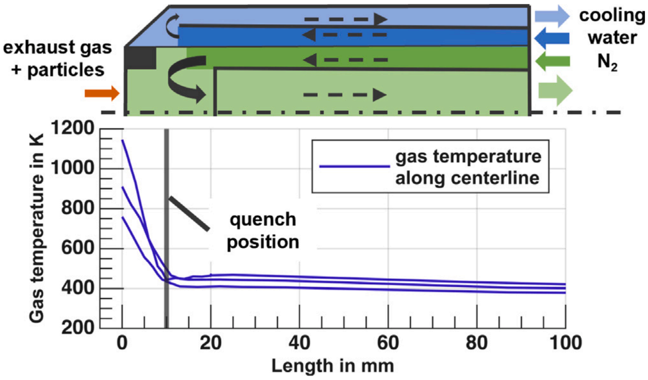

Fig. 4. A cross section and the corresponding gas temperatures determined on the center line of the extraction probe with a thermocouple during operation are shown. The different temperature curves result from different extraction conditions used for particle extraction. The quench position of 10 mm is indicated.

A type K thermocouple (TC) positioned directly in front of the filter indicated a constant gas temperature below 354 K in the filter. To determine the quenching conditions, the internal gas temperature along the center line of the particle extraction probe was determined using another type K TC in an additional measurement. This TC had an outer diameter of 3 mm. Central alignment was ensured with a distance holder added to the TC. Three measured center line temperature curves are shown in Fig. 4 together with a cross section of the extraction lance tip. A change in the temperature gradient was observed in the gas temperatures 10 mm downstream the inlet due to the entrance of the quench gas. It is indicated in Figs. 2 and 4 as quench position (d_q). Further downstream the gas temperature was below 473 K. The distance between the burner surface and this change in temperature gradient was defined as the relevant HAB for sampling and was assumed to be the distance at which particles were quenched. The deviations in the three temperature curves result from slight changes in the extraction conditions used to achieve a similar particle deceleration at the inlet of the extraction probe. Considering the measured initial quench gas temperature and the gas mass flow, the initial average quench gas velocity was up to 17 m/s leading to a significant particle acceleration during quenching.

The cooling rate of a 49 μm particle was estimated to be in the order of 1×10^5 K/s assuming constant material properties for solid FeO at a constant intermediate particle temperature of 1600 K. For the used particles size of 35 to 60 μm, the estimated cooling rate was between 2×10^5 K/s and 7×10^4 K/s. Therefore, the particle oxidation is considered to be rapidly terminated within the extraction probe.

To examine the overall reproducibility of the sampling and subsequent phase determination, three samples were additionally collected at a selected sampling position and their oxide composition was determined with WAXS and MS. The standard deviation of the detected oxide composition was determined to be $8\,\%_{\text{mass}}$ for WAXS and $5\,\%_{\text{mass}}$ for MS.

To determine the sensitivity of particle oxidation to the gas composition within the extraction probe, one measurement was performed by adding $1\,\%_{\text{vol}}$ O_2 to the quench gas, and another one was performed by exposing the particles to the (warm) quench gas in the filter for additional two hours. The variation found in the different oxides was in the order of one standard deviation of the overall reproducibility or even less and is therefore considered insignificant. Therefore, the probing is considered insensitive to small variations in the quench gas composition, and to the residence time of the sampled particles in the filter during the extraction.

2.5. Two-color pyrometry

To correlate the *ex-situ* determined oxidation state with the combustion progress, the particle temperature evolution was measured *in-situ* using a two-color pyrometry system shown in Fig. 2(b). The system mainly consisted of a 50:50 beam splitter cube and two time-synchronized high-speed cameras (Photron SA-X2). Each camera was equipped with a macro objective lens (Sigma 105 mm $f/2.8$). The equally split thermal radiation emitted from the isolated burning particles was filtered by 850 ± 25 nm and 950 ± 25 nm interference filters and then recorded by the cameras, respectively. Since the cameras were more sensitive at around 850 nm, a neutral density filter (OD = 0.6) was used to balance the pixel intensities at a similar level when the particle reached its peak temperature. To avoid camera saturation and maximize the optical signal, the images were defocused by moving the LFR 3 mm away from the focal plane and identical exposure times (40 μs) were empirically selected for both cameras. The field of view (FOV) of the pyrometer was aligned axially with the burning particle streaks. The integrated radiative intensities of the particles were reconstructed by binning at least 50 connected background-subtracted pixels constituting the particle images, reducing the influence of noise (average background corrected noise level on each sensor of 1.6 counts) onto the determined particle luminosity. The ratio between the radiative intensities at two wavelengths are related with the particle surface temperature by

$$\frac{S_{\lambda_1}}{S_{\lambda_2}} = \Gamma^{\text{cal}} \left(\frac{\varepsilon_1}{\varepsilon_2}\right) \left(\frac{\lambda_2}{\lambda_1}\right)^5 \frac{e^{(c_2/\lambda_2 T)} - 1}{e^{(c_2/\lambda_1 T)} - 1}, \tag{1}$$

where S_{λ_i}, ε_i are the radiative intensity and emissivity at wavelength λ_i and surface temperature T, respectively, c_2 is the second radiation constant, Γ^{cal} is the instrument factor that was determined by calibration. A single burning iron particle is treated as a gray body and it is assumed that $\varepsilon_1/\varepsilon_2 = 1$. The particle temperature was obtained by solving Eq. (1) iteratively following the approach in [14].

According to the measurement of Kobatake et al. [15], the spectral emissivity of liquid iron has a weak negative wavelength dependence and negligible temperature dependence in the range of 780–920 nm (measurements only conducted in this range). This measurement agrees very well with the calculation of the Drude model. Based on this model, the emissivity of liquid iron at 850 nm and 950 nm are 0.38 and 0.37, respectively. The neglection of the difference between emissivity in the two-color pyrometry causes a 50 K overestimation for the melting point of iron (1809 K). During liquid phase combustion, the outer surface of the particle is likely covered by a layer of liquid iron oxide, as suggested by the morphology of quenched particles (see Section 3.4). However, due to the lack of information on the spectral emissivity of liquid iron oxide, the error in the surface temperature measurement, introduced by the graybody assumption, cannot be estimated. Based on the good agreement between the archived solidification temperature of liquid iron oxide with the pyrometric measurement using graybody assumption [5] the wavelength dependence of the emissivity of liquid iron oxide is likely not significant.

The instrument factor Γ^{cal} was calibrated using a NIST-certified tungsten lamp over a wide temperature range, 1346–2915 K. For a given lamp temperature T_{lamp}, the signal intensity S_{λ_i} at around 850 nm (λ_1) and 950 nm (λ_2) were obtained by binning pixels within a 10 × 10 window located at the center of the imaged lamp strip. The spectral emissivity of tungsten ε_i at λ_i reported in [16] was used to calculate the theoretical emission intensity of the tungsten strip lamp based on Planck's law. Substituting the corresponding S_{λ_i} and ε_i at multiple T_{lamp} into Eq. (1), $\Gamma^{\text{cal}} = 1.15$ was obtained by the least-squares fitting. The 95% confidence interval of the fitting is 0.002, corresponding to an absolute error less than 25 K at a temperature below 3100 K.

More than 300 burning particles were imaged using the two-color pyrometry system, providing the temporally and spatially resolved histories of the filtered particle luminosities at around 850 and 950 nm. Thereafter, the particle temperatures were derived as a function of residence time and also HAB. The determined temperatures and corresponding residence times of the particles along HAB were binned within 1 mm width of HAB. At a fixed HAB, particles with temperatures exceeding ±3 times the standard deviation were considered as outliers and removed, corresponding to a maximum of 2 % of the determined number of particles measured at a single HAB. This particle-binning procedure gives an average particle temperature history as a function of HAB and also as a function of time with the reference time t_0 defined at the peak of the particle-averaged temperature. The particle temperature could only be determined for the peak temperature region due to a low signal-to-noise ratio afterwards.

2.6. ^{57}Fe Mössbauer spectroscopy

MS was performed at room temperature using a home-built setup consisting of a velocity drive unit from Halder instruments, a proportional counter as detector, a preamplifier, an amplifier, and a CMCA-500 unit (Wissel) for discrimination and data acquisition. The ^{57}Co/Rh source had an initial activity of 100 mCi and was continuously kept at room temperature. The source was moved in a triangular waveform. A 25 μm thick α-iron foil was used as calibration standard. Fitting of the experimental data was performed with the MossA software package, solving the full transmission integral [17], resulting in the fitting parameters given in Table S1. Uncertainties in compositions were determined from fitting errors. Conversion of spectral area to relative sample composition was achieved with Lamb-Mössbauer factors as presented in Spielmann et al. [18]. Measured Mössbauer spectra are given in Fig. S2. Sample loadings were in the range of 35 to 45 mg/cm^2. Single measurements were performed for samples split from the probed particles at each HAB.

2.7. Wide-angle X-ray scattering

WAXS is a measurement method for a qualitative and quantitative phase analysis which is based on the interaction of X-rays and matter. In a crystalline material, this interaction leads to diffraction phenomena, known as X-ray diffraction. The experiments were conducted using a laboratory SWAXS beamline, a Xeuss 2.0 Q-Xoom (Xenocs SA, Grenoble, France). X-rays were generated by an X-ray source (GeniX 3D Cu ULD) that emits Cu-K$_\alpha$ radiation. The wavelength of the X-rays used in this study was 1.5406 Å. The (unmilled) powder sample, consisting of oxidized iron particles, was placed on an adhesive polyimide foil allowing the controlled exposure of the sample to the collimated beam. The sample-to-detector distance was maintained at 80 mm throughout the experiments. The diffraction patterns obtained from the Pilatus3 R 300k detector were utilized for further analysis. In this way, characteristic Bragg peaks in the diffraction pattern were identified and analyzed to extract the averaged mass fraction of each crystalline phase identified in the powder samples. For the evaluation of the interference peaks, the IR method was applied, which is discussed in previous work [19]. Here, it has also been shown, that, compared to X-ray diffraction (XRD), all necessary Bragg-peaks are detected in the WAXS setup. The diffraction patterns measured in the work are presented in Fig. S3. The peaks used for the particle evaluation are marked. Independent measurements were conducted for three sub-samples split from the particles extracted at each HAB. The measurement uncertainty was then determined as the standard deviation of the three measurements.

2.8. Microscopy and atomic distribution

To gain insights into the morphology of the partially oxidized particles, a scanning electron microscope (FEI Helios G4) equipped with focused ion beam (FIB) was utilized. Using FIB, selected particles were cut precisely to expose cross-sectional areas, allowing for the analysis of the internal structures of the particles. Energy-dispersive X-ray spectroscopy (EDX) was employed to differentiate between the iron and iron oxide phases.

3. Results and discussion

3.1. Overall oxidation progress

Fig. 5(a) shows the O:Fe mole ratio (n_O/n_{Fe}) of the sampled particles, derived from the composition measured by MS and WAXS. For reference, the O:Fe mole ratios of (3) pure FeO ($n_O/n_{Fe} = 1$), (2) Fe_3O_4 ($n_O/n_{Fe} = 1.33$), and (1) Fe_2O_3 ($n_O/n_{Fe} = 1.5$) are marked by horizontal dotted lines. In addition, the position of the particle peak temperature is marked (vertical dot-dashed lines) with its corresponding standard deviation (vertical dashed lines). Notably, a significant increase in the O:Fe mole ratio occurs in the early stages up to about 50 mm HAB, which levels off at a ratio corresponding to Fe_3O_4. Similar reaction characteristics have been described for low-temperature oxidation before [20]. Both WAXS and MS show similar trends in the overall oxidation progress.

Fig. 5(b) zooms into the region with the fastest increase in O:Fe mole ratio and correlates the oxidation rate with the reaction time t_r relative to the peak temperature, instead of HAB. For reference, the corresponding HAB at a given reaction time, relative to the peak temperature, is provided on the top x-axis. Additionally, averaged gas T_{gas} and particle T_{prt} temperatures are depicted, emphasizing on the region of elevated particle surface temperatures and a rapid reaction progress The measured particle temperatures are averaged for a given HAB and the system detects all micron sized particles. This results in a lower average peak temperature and a flatter temperature profile. Notably, the peak of T_{prt} is reached at a ratio of close to FeO ($n_O/n_{Fe} = 1$), but an exact correlation cannot be made due to measurement uncertainties. Due to the weak signal at low particle temperatures, the particle velocities were measured only up to 140 mm. Therefore, the conversion of the spatial domain into a time domain was limited to $\overline{t_r} =$ 172 ms. Thus, it was not possible to convert the entire spatial domain into a time domain. Therefore, HAB is consistently used throughout the following discussion.

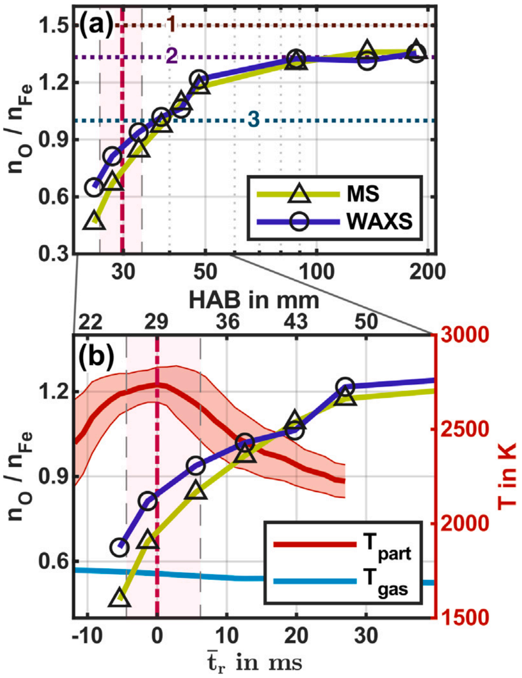

Fig. 5. (a) Overall oxidation progress shown as oxygen–iron ratio compared to the ratio the pure oxides (horizontal dashed lines). Position of the peak temperature is given as a vertical dashed line. (b) Particle surface and gas temperatures are given in correlation to the overall oxidation progress relative to time and HAB. Gas temperatures are taken from [12].

The particle temperature and reaction times were determined in absence of the extraction probe. The influence of the extraction probe on the particle sampling is minimized but likely present. One the one hand, the likely reduced oxygen content in the first 10 mm of the extraction probe and the lower gas phase temperature reduces the particle reaction rate. Therefore, the resulting particle compositions correspond to lower HABs. On the other hand, the probe slightly reduces particle velocities, which is associated with increased residence times. This effect causes particle compositions corresponding to slightly higher HABs. The extent to which these opposing effects balance each other out remains an open question.

3.2. Phase resolved oxidation progress

Fig. 6 shows the overall mass fractions of α-Fe, FeO, Fe_3O_4, and Fe_2O_3 within the sampled particles at different HABs, determined by WAXS and MS, independently. Again, peak particle temperature and its standard deviations are indicated for reference. The corresponding mean reaction time relative to the peak temperature is indicated at the top. Due to the specific characteristics of the methods used, the error bars given for the MS measurements represent fitting errors, while those for the WAXS data indicate the standard deviation of the determined oxide composition of three subsamples of the same sample.

The progresses of each phase follow a distinct pattern. First, elemental iron undergoes complete oxidation and disappears above a HAB of 48 mm. Along with the Fe consumption, the FeO content increases and peaks first among all oxides, followed by the appearance of the Fe_3O_4 peak. At an even later stage, Fe_2O_3 is formed first in the sample extracted at 137 mm HAB. Notably, the peak of FeO formation is close to the region of highest particle surface temperature, indicated by the vertical dashed lines. The peak T_{prt} is slightly shifted relative to the FeO peak, however, a reasonable alignment between both is still evident considering measurement uncertainties.

Moreover, both methods provide similar results for capturing the oxidation progress, namely, the average degree of oxidation changes

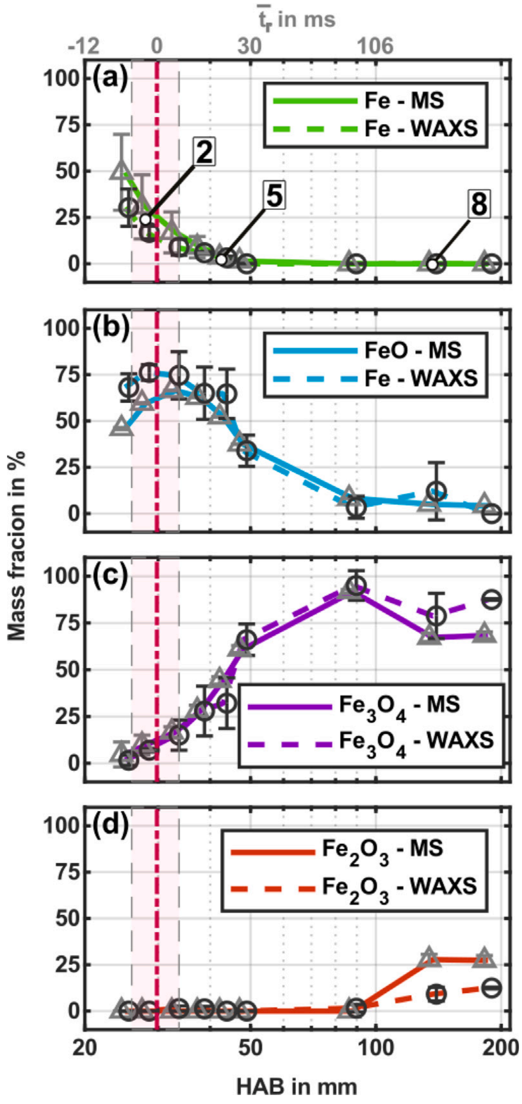

Fig. 6. Mass fraction of α-Fe (a) and its oxides (b–d). Error bars for the MS results indicate the fitting error. For WAXS the error bars indicate the standard deviation of three sub-samples analyzed from the same sample. Points are shifted slightly from each other in horizontal direction for better visibility. Numbers in (a) indicate the positions from which particles were analyzed with SEM (see Fig. 7). Mean reaction time relative to the peak temperature (vertical dashed line) is indicated at the upper x-axis.

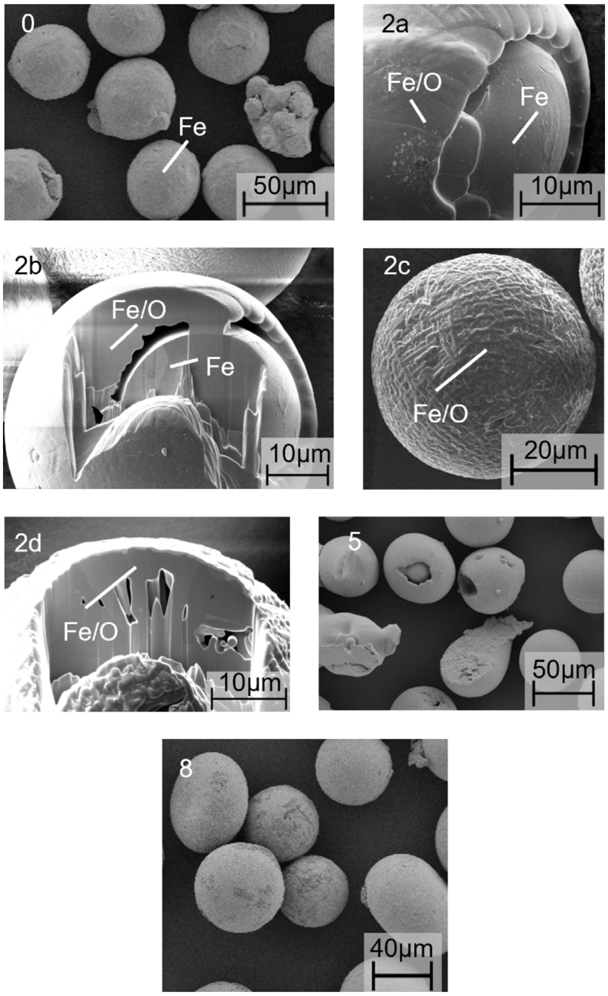

Fig. 7. SEM images of the sampled particles. Sampling positions are: (0) original, (2a–d) 28 mm, (5) 43 mm, and (8a–b) 137 mm HAB. (2b, d) are sections of the particles (2a, c) cut with FIB. The numbering of the images indicates the sampling position in Figs. 6 and 8.

qualitatively in a similar manner over HAB. However, the phase composition, from which the degree of oxidation is determined, has some distinct differences that will be discussed below.

3.3. Differences between WAXS and MS measurements

At low heights, both measurements indicate the presence of residual iron in the particles. This is confirmed by the FIB-SEM images and EDX in Fig. 7 (2a, b), showing individual particles with an enclosed iron core. Despite the decreasing trend of Fe evidenced by both measurement methods, WAXS measurements quantitatively identify smaller mass fractions of iron (and correspondingly higher mass fractions of FeO) compared to the phase analysis using MS. This difference is likely due to the particle size and the heterogeneous structures of the oxides. A 40–50 µm partially oxidized particle exhibits a core–shell structure, in which an iron core is enclosed by an oxide shell. When X-rays interact with this structure, according to the Beer–Lambert law, a portion is absorbed. Dependent on the linear absorption coefficient, the radiation is attenuated exponentially over the penetration depth of the X-rays. In case of the present WAXS setup, which utilizes Cu-K$_\alpha$ radiation (E = 8.047 keV), pure iron has a mass absorption coefficient of 228.5 cm^2 g^{-1} [21]. This results in a transmission of approximately 16.5 % at a penetration depth of 10 µm and approximately 1.1 % at 25 µm, which is roughly half the particle diameter. Since only the transmitted portion of the radiation leads to measurable scattering effects, the interior of a particle is underrepresented in WAXS. Given a heterogeneous structure such as the observed core–shell structure, the scattering effects of the shell dominate, leading to a systematic deviation at lower HABs. In contrast, MS utilizes electromagnetic radiation at shorter wavelengths (E = 14.413 keV), resulting in a smaller linear absorption coefficient and greater transmission over the penetration depth. This allows for a better accessibility to the core and thus the larger Fe mass fractions at lower HAB. Nevertheless, further investigations with regards to the deviations observed in different measurements are desired, especially for the deviation in Fe_2O_3 mass fraction at higher HAB.

3.4. Morphology and inner structure

SEM images were recorded for the original iron particles and for partially combusted particles at different HAB. The influence of the cooling onto the visible morphology needs to be considered in the analysis of the images.

An influence of the cooling rate on the morphology is described in the literature but quantitative cooling rates are sparse. The authors are not aware of reported cooling rates for combusting iron particles. Dreizin shows that slow cooling of combusting Zi particles with a rate of about $\sim 10^4$ K/s lead to the formation of oxygen rich and oxygen poor regions and small voids in the particles. Those were not visible for particles cooled with a fast rate of about $\sim 10^6$ K/s and must have been formed during the cooling [11]. Muller et al. shows that for burning iron rods with a diameter of 3 mm, the solidified boundary between the oxygen depleted liquid iron phase (L1) and the oxygen enriched liquid iron phase (L2) is smooth for slowly quenched rods whereas it is wrinkled for rods quenched faster by interaction with a copper plate [22]. This indicates a smoothing of the interfacial boundary during slow cooling.

The cooling rate achieved in this work of $\sim 1 \times 10^5$ K/s is in between the two rates reported by Dreizin for Zi particles but similar to that reported by Dreizin for ~250 μm Cu particles [11,23]. Here, Dreizin reports the formation of an oxide layer during combustion and the formation of spherical oxide inclusions in the copper core, due to a slow cooling rate leading to a partial separation between Cu and its oxides. Notably, the particle has burned at a temperature above the miscibility gap and therefore it has been in a single liquid phase during combustion.

A number of studies have been performed, in which iron particles have been sampled and analyzed before showing that collected particles contain cracks and porosities [10,24] or that they form a hollow shell at later combustion stages [7,8,25]. Different explanations have been proposed for the formation of these porosities. They were described as either shrinkage holes, the results of different gas species (O_2, N_2, CO, CO_2) diffusing into the molten particle during combustion or caused by the evaporation of small portions of iron from the center of the particle [8–10,24]. Here, they form gas bubbles, which may nucleate and lead to either nano-particles, cracked shells or inflated shells. Notably, it is known that more O_2 can be dissolved in L2 at higher temperatures, which might lead to the outgassing of excess oxygen and the corresponding formation of O_2 filled pores during cool down [26]. Impurities in the iron particles may also react and contribute to the porosities [8].

Exemplary results for the iron particles extracted in this work are shown in Fig. 7, originating from the corresponding sampling positions (SP) highlighted in Fig. 6(a) with numbers. Original iron particles depicted in Fig. 7 (0) are predominantly spherical in shape with some attached smaller particles and dent-like structures. For the particles extracted at SP 2 of 28 mm HAB, shown in Fig. 7 (2a-d), the particles exhibit a spherical structure, indicating that they have been melted. This is supported by the measured particle temperature of ~2730 K.

Notably, two distinct particle types are identified: those with a core surrounded by a smooth shell in Fig. 7 (2a, 2b) and those with a more rough surface without detectable core in Fig. 7 (2c, 2d). FIB cutting of these particles reveals their inner structures in Fig. 7 (2b, 2d), respectively. In Fig. 7 (2b), a shell encapsulates a spherical core that is asymmetric with respect to the particle center, and in particular there is a gap between the core and the shell, but no porosity in either the shell or the core. Using qualitative EDX, the composition of the shell is determined to be an iron–oxygen mixture, and the composition of the core is determined to be almost pure iron. Considering the measured particle temperature of around 2730 K at the sampling location and the very small Biot number, the particle was fully molten and separated into two liquid phases, suggested by the two-phase region, consisting of L1 and L2, of the Fe–O phase diagram (see Fig. 8, Region L1+L2), in which SP 2 is positioned. During cooling, first L1 solidifies to δ-Fe due to the higher solidification temperature, forming the core. Afterwards the L2 solidifies. As a small negative temperature gradient along the particle radius is expected, the exterior of the L2 phase may solidify first, forming a shell. Considering the results from Muller et al., the surfaces of the core and the shell might have smoothed during the cooling [22]. Since the volume of L2 shrinks during solidification, the later solidification of interior L2 probably creates a porosity, apparent as the gap in Fig. 7 (2b). Dissolved gas species, formed bubbles and small amounts of evaporated L1 and L2 inside the particle may also contribute to the formation of the gap. Due to surface tension, L2 could contract towards one side before and during solidification, forming a naturally open shell visible in Fig. 7 (2a, 2b). In addition, the particles experience a significant acceleration at the quench gas inlet in the extraction probe which may also contribute to the asymmetry of the shell and the core with respect to the particle center.

The presence of the core–shell structure in the quenched particle suggests that L1 and L2 are layered during liquid phase combustion. At SP 2 the mean particle temperature is 2730 K, which is above the experimentally validated composition of the Fe–O phase diagram of around 2300 K. The calculated binodal curve indicates a required temperature of more than 2900 K with respect to the determined oxygen concentrations at SP2 to leave the miscibility gap and form a single liquid. Less than 3 % of the measured particle temperature trajectories exceeded this temperature. Therefore, the core–shell structure has likely formed already during oxidation and is not considered to be a result of the particle cooling. To our knowledge, such iron-core and oxide-shell structures were observed for rapidly quenched, partially oxidized iron particles for the first time.

The second type of particles that are observed and exemplified in Fig. 7 (2c) contain porosities, as detailed in Fig. 7 (2d). EDX reveals its composition as iron-oxygen mixture. The differences between these two particles are likely caused by slight differences in the reaction times. A similar porous structure was reported by Choisez et al. [10], which was explained either by the volume shrinkage or internal gas release during solidification of the particles.

Particles extracted at a HAB of 43 mm, shown in Fig. 7 (5), have a spherical shape and a much smoother surface compared to Fig. 7 (2c). Some particles exhibit a core–shell structure or might have been deformed by collisions with the extraction probe. Such particles with large pores have been reported in literature before [10,24,25]. Advancing to 137 mm, particles shown in Fig. 7 (8) resemble those from 43 mm. Interestingly, fewer particles displayed large holes in the shell compared to Fig. 7 (5). The different surface structures compared to samples in Fig. 7 (2) is probably caused by different resolutions between the devices used for SEM and FIB-SEM.

3.5. Mapping oxidation trajectory onto Fe–O phase diagram

The Fe–O equilibrium diagram was created using FactSage 8.3 [27]. Here, the phase diagram was calculated using the Phase Diagram module and the following solution phases: gas, Fe-liq, BCC-A2, FCC-A1, A-Liq(Matte/Metal), A-Monoxide, A-Spinel, Fe2O3(s). Characteristic points in the diagram were compared to experimental values reported by Hidayat et al. [28]. Experimental data are only reported up to around 2300 K and, therefore all data for temperatures above this are computed only.

The determined overall mole ratio and the temperature of the particle sampled at different HAB are mapped onto the Fe–O equilibrium phase diagram. Due to the lack of temperature information at HAB $>$ 50 mm, only a temperature range is given for SP 7–9, which is estimated to be between the extrapolated gas temperature and the farthest downstream particle temperature measured at SP 6. The SP with their corresponding HAB are summarized in Table 1.

Fig. 8 shows that SP 1–3 are all in the two-phase region, consisting of L1 and L2, followed by the particles from SP 4–6 in the L2 region. Elemental α-Fe can be detected up to SP 5, as observed consistently in Fig. 6. In addition, significant amounts of FeO can be found in SP 1–7 (see Fig. 6). This suggests that during the fast cooling process of the quenched particles, metastable FeO was formed, which is consistent with the observation reported in [28]. Fe_2O_3 is detected in particles from SP 8–9, with slight variations in particle composition due to

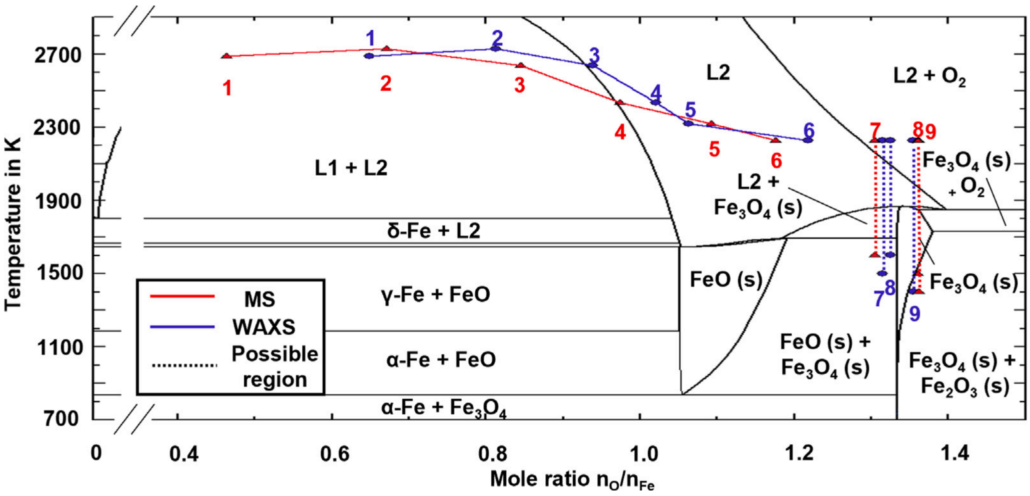

Fig. 8. Equilibrium phase diagram of Fe–O created with FactSage [27]. The *in-situ* measured particles temperatures are combined with *ex-situ* mole ratios determined with MS and WAXS. Due to temperature measurements limited to positions up to SP 6, for SP 7–9, only temperature ranges can be estimated, indicated by dotted lines. The corresponding HAB for each sampling position are summarized in Table 1.

Table 1
Sampling positions with corresponding heights above burner.

Sampling position (SP)	Height above burner (HAB)
0	educt
1	25 mm
2	28 mm
3	33 mm
4	38 mm
5	43 mm
6	48 mm
7	88 mm
8	186 mm

different trajectories with respect to SP 8 for WAXS. This is consistent with the phase diagram findings that cooling particles sampled at SP 8–9 below ~1100 K yields a fraction of Fe_2O_3 in the particles.

The found core–shell structure and the mapped positions of the SP 1–3 in the miscibility gap of L1 and L2 in the Fe–O phase diagram support the concept of a core–shell structure during liquid phase combustion. Such a core–shell structure during liquid phase combustion has been assumed before, e.g by Fujinawa et al. [29]. However, the experimental observations also show deviations from point-symmetric core–shell structures and the formation of pores with complex topologies. These findings are relevant for refining modeling or iron particle combustion in the future.

4. Conclusions and outlook

The oxidation progress of single micron-sized iron particles during combustion in a hot atmosphere with 20 $\%_{vol}$ O_2 was studied under well-defined thermal and aerodynamic boundary conditions. The particles were sampled with an extraction probe that rapidly quenched the particles to prevent further oxidation. This allowed to combine the *in-situ* measured combustion parameters, including gas temperature, particle surface temperature, and particle residence time, with the internal particle properties determined *ex-situ* such as oxide composition and particle morphology. It was shown that the particle oxidation can be divided into two phases, an initial phase with fast oxidation followed by a second much slower oxidation phase. During the initial fast phase, the particles heated up to the peak temperature, and the Fe was almost completely consumed. In the quenched particles, the FeO peak was observed during the initial phase, followed by a Fe_3O_4 peak during the slower oxidation phase. Formation of Fe_2O_3 started at the end of the involved residence time.

Two types of morphologies were observed on the SEM images taken from particles during the initial rapid heating phase. First, a core–shell structure was identified with a smooth shell consisting of iron oxide and a smooth spherical core consisting mainly of iron. Second, a particle without a visible core was observed at the same position, but with a much rougher surface, probably due to slight differences in oxidation levels. For particles extracted in the second, slower oxidation phase, particles with open holes in the shells were more frequently observed at lower HAB, depending on the sampling position.

This work provides valuable data for the CFD modeling of single particle oxidation by the combination of *in-situ* measured time resolved particle temperatures and *ex-situ* measured particle oxidation progress in a well defined hot gas environment. In addition, the seen particle morphology of an iron oxide shell around an iron core indicates that single particles initially burn in a shell structure. Deviations from spherical symmetry of the core–shell structure, along with the formation of pores, were also noted.

These findings provide important insights for future model improvements. For example, investigating whether internal flows, induced by slip velocity, contribute to the observed asymmetry between core and shell. Additionally, understanding the transport properties of ions within liquid iron oxide could offer deeper insights into the oxidation process of core–shell particles. Including pore formation during combustion may also enhance current models. To better validate such models, a more extensive statistical analysis involving a larger number of particles is needed.

In addition, measurements of wide emission spectra of iron particles and iron oxide particles at temperatures above 2300 K will provide valuable information on the wavelength dependence of the emissivity. This information can then be used to improve the two-color pyrometry measurements and further quantify the impact of the graybody assumption, for example by applying the method described by Long et al. [30].

CRediT authorship contribution statement

Anton Sperling: Writing – original draft, Visualization, Methodology, Investigation, Formal analysis, Data curation, Conceptualization. **Max P. Deutschmann:** Writing – review & editing, Writing – original draft, Investigation. **Daoguan Ning:** Writing – review & editing, Writing – original draft, Software. **Jonas Spielmann:** Writing – review & editing, Writing – original draft, Investigation, Data curation. **Tao Li:** Writing – review & editing. **Ulrike I. Kramm:** Writing – review & editing, Supervision, Funding acquisition. **Hermann Nirschl:** Writing –

review & editing, Supervision, Funding acquisition. **Benjamin Böhm:** Writing – review & editing, Supervision, Funding acquisition. **Andreas Dreizler:** Writing – review & editing, Supervision, Funding acquisition.

Declaration of competing interest

The authors declare that they have no known competing financial interests or personal relationships that could have appeared to influence the work reported in this paper.

Data availability

Data will be made available on request.

Acknowledgments

The helpful discussions with J. Mich and T. Krenn is gratefully acknowledged. We acknowledge V. Zibat and Dr. E. Müller (Laboratory for Electron Microscopy, KIT) for their help with SEM, FIB, and EDX. This work was performed within the cluster project Clean Circles, co-funded by the Hessian Ministry of Higher Education, Research, Science, and the Arts and the Strategy Fund of the KIT Presidium.

Appendix A. Supplementary material

The corresponding MS fitting parameters and spectra, and the WAXS diffraction pattern are provided in the supplementary material.

Supplementary material related to this article can be found online at https://doi.org/10.1016/j.fuel.2024.133147.

References

[1] Bergthorson JM, Goroshin S, Soo MJ, Julien P, Palecka J, Frost DL, et al. Direct combustion of recyclable metal fuels for zero-carbon heat and power. Appl Energy 2015;160:368–82. http://dx.doi.org/10.1016/j.apenergy.2015.09.037.

[2] McRae M, Julien P, Salvo S, Goroshin S, Frost DL, Bergthorson JM. Stabilized, flat iron flames on a hot counterflow burner. Proc Combust Inst 2019;37(3):3185–91. http://dx.doi.org/10.1016/j.proci.2018.06.134.

[3] Ning D, Shoshin Y, van Oijen JA, Finotello G, de Goey L. Burn time and combustion regime of laser-ignited single iron particle. Combust Flame 2021;230. http://dx.doi.org/10.1016/j.combustflame.2021.111424.

[4] Li S, Huang J, Weng W, Qian Y, Lu X, Aldén M, et al. Ignition and combustion behavior of single micron-sized iron particle in hot gas flow. Combust Flame 2022;241:112099. http://dx.doi.org/10.1016/j.combustflame.2022.112099.

[5] Ning D, Shoshin Y, van Stiphout M, van Oijen J, Finotello G, de Goey P. Temperature and phase transitions of laser-ignited single iron particle. Combust Flame 2022;236:1–11. http://dx.doi.org/10.1016/j.combustflame.2021.111801.

[6] Panahi A, Chang D, Schiemann M, Fujinawa A, Mi X, Bergthorson JM, et al. Combustion behavior of single iron particles-part I: An experimental study in a drop-tube furnace under high heating rates and high temperatures. Appl Energy Combust Sci 2023;13:100097. http://dx.doi.org/10.1016/j.jaecs.2022.100097.

[7] Sepman A, Malhotra JS, Wennebro J, Wiinikka H. Iron as recyclable electrofuel: Effect on particle morphology from multiple combustion-regeneration cycles. Combust Flame 2024;259:113137. http://dx.doi.org/10.1016/j.combustflame.2023.113137.

[8] Huang J, Wu Z, Cai W, Berrocal E, Aldén M, Li Z. Volume expansion and micro-explosion of combusting iron particles analyzed using magnified holographic imaging. Powder Technol 2023;420:118412. http://dx.doi.org/10.1016/j.powtec.2023.118412.

[9] Li Y-H, Purwanto A, Chuang B-C. Micro-explosion mechanism of iron hybrid methane-air premixed flames. Fuel 2022;325:124841. http://dx.doi.org/10.1016/j.fuel.2022.124841.

[10] Choisez L, van Rooij NE, Hessels CJ, Da Silva AK, Filho IRS, Ma Y, et al. Phase transformations and microstructure evolution during combustion of iron powder. Acta Mater 2022;239:118261. http://dx.doi.org/10.1016/j.actamat.2022.118261.

[11] Dreizin EL. Phase changes in metal combustion. Prog Energy Combust Sci 2000;26(26):57–78. http://dx.doi.org/10.1016/S0360-1285(99)00010-6.

[12] Li T, Farmand P, Geschwindner C, Greifenstein M, Köser J, Schumann C, et al. Homogeneous ignition and volatile combustion of single solid fuel particles in air and oxy-fuel conditions. Fuel 2021;291:120101. http://dx.doi.org/10.1016/j.fuel.2020.120101.

[13] Tarlinski D, Geschwindner C, Li T, Böhm B, Schiemann M. Particle temperature and composition measurements in the ignition phase of single coal particles and particle groups under conventional and oxy-fuel atmospheres. Fuel 2023;332:125894. http://dx.doi.org/10.1016/j.fuel.2022.125894.

[14] Levendis YA, Estrada KR, Hottel HC. Development of multicolor pyrometers to monitor the transient response of burning carbonaceous particles. Rev Sci Instrum 1992;63(7):3608–22. http://dx.doi.org/10.1063/1.1143586.

[15] Kobatake H, Khosroabadi H, Fukuyama H. Normal spectral emissivity measurement of liquid iron and nickel using electromagnetic levitation in direct current magnetic field. Metall Mater Trans A 2012;43(7):2466–72. http://dx.doi.org/10.1007/s11661-012-1101-0.

[16] Pon RM, Hessler JP. Spectral emissivity of tungsten: analytic expressions for the 340-nm to 2.6-microm spectral region. Appl Opt 1984;23(7):975–6. http://dx.doi.org/10.1364/AO.23.000975.

[17] Prescher C, McCammon C, Dubrovinsky L. Mossa: a program for analyzing energy-domain mössbauer spectra from conventional and synchrotron sources. J Appl Crystallogr 2012;45(2):329–31. http://dx.doi.org/10.1107/S0021889812004979.

[18] Spielmann J, Braig D, Streck A, Gustmann T, Kuhn C, Reinauer F, et al. Exploring the oxidation behavior of undiluted and diluted iron particles for energy storage: Mössbauer spectroscopic analysis and kinetic modeling. Phys Chem Chem Phys PCCP 2024;26(17):13049–60. http://dx.doi.org/10.1039/d3cp03484d.

[19] Buchheiser S, Deutschmann MP, Rhein F, Allmang A, Fedoryk M, Stelzner B, et al. Particle and phase analysis of combusted iron particles for energy storage and release. Materials (Basel, Switzerland) 2023;16(5). http://dx.doi.org/10.3390/ma16052009.

[20] Korshunov AV. Kinetics of the oxidation of an electroexplosion iron nanopowder during heating in air. Russ J Phys Chem B 2012;6(3):368–75. http://dx.doi.org/10.1134/S1990793112050053.

[21] Hubbell J, Stephen Seltzer. Tables of X-Ray mass attenuation coefficients and mass energy-absorption coefficients 1 kev to 20 MeV for elements Z=1 to 92 and 48 additional substances of dosimetric interest. 1995.

[22] Muller M, El-Rabii H, Fabbro R. Liquid phase combustion of iron in an oxygen atmosphere. J Mater Sci 2015;50(9):3337–50. http://dx.doi.org/10.1007/s10853-015-8872-9.

[23] Dreizin EL. Effect of phase changes on metal-particle combustion processes. Combust Explos Shock Waves 2003;2003(39):681–93. http://dx.doi.org/10.1023/B:CESW.0000007682.37878.65.

[24] Wiinikka H, Vikström T, Wennebro J, Toth P, Sepman A. Pulverized sponge iron, a zero-carbon and clean substitute for fossil coal in energy applications. Energy Fuels 2018;32(9):9982–9. http://dx.doi.org/10.1021/acs.energyfuels.8b02270.

[25] Li Y-H, Pangestu S, Purwanto A, Chen C-T. Synergetic combustion behavior of aluminum and coal addition in hybrid iron-methane-air premixed flames. Combust Flame 2021;228:364–74. http://dx.doi.org/10.1016/j.combustflame.2021.02.013.

[26] Steinberg TA, Mulholland GP, Benz FJ. The combustion of iron in high-pressure oxygen. Combust Flame 1992;1992(89):221–8. http://dx.doi.org/10.1016/0010-2180(92)90030-S.

[27] Bale CW, Bélisle E, Chartrand P, Decterov SA, Eriksson G, Gheribi A, et al. FactSage thermochemical software and databases - 2010 - 2016. CALPHAD 2016;54:35–53, URL www.factsage.com.

[28] Hidayat T, Shishin D, Jak E, Decterov SA. Thermodynamic reevaluation of the Fe–O system. CALPHAD 2015;48:131–44. http://dx.doi.org/10.1016/j.calphad.2014.12.005.

[29] Fujinawa A, Thijs LC, Jean-Philyppe J, Panahi A, Chang D, Schiemann M, et al. Combustion behavior of single iron particles, Part II: A theoretical analysis based on a zero-dimensional model. Appl Energy Combust Sci 2023;14:1–16. http://dx.doi.org/10.1016/j.jaecs.2023.100145.

[30] Long BA, Rodriguez DJ, Lau CY, Schultz M, Anderson SL. Thermal emission spectroscopy of single, isolated carbon nanoparticles: Effects of particle size, material, charge, excitation wavelength, and thermal history. J Phys Chem C 2020;124(2):1704–16. http://dx.doi.org/10.1021/acs.jpcc.9b10509.